

Non-bonding Interaction of Dual Atom Catalysts for Enhanced Oxygen Reduction Reaction

Mohsen Tamtaji,¹ Qiuming Peng,² Tongchao Liu,³ **Xue Zhao**,² **Zhihang Xu**,⁴ Patrick **Ryan** Galligan,¹ Md Delowar Hossain,¹ Zhenjing Liu,¹ Hoilun Wong,¹ Hongwei Liu,¹ Khalil Amine,³ Ye Zhu,^{4*} William A. Goddard III,^{5*} Wenting Wu,^{6*} and Zhengtang Luo,^{1*}

¹Department of Chemical and Biological Engineering, Guangdong-Hong Kong-Macao Joint Laboratory for Intelligent Micro-Nano Optoelectronic Technology, William Mong Institute of Nano Science and Technology, and Hong Kong Branch of Chinese National Engineering Research Center for Tissue Restoration and Reconstruction, The Hong Kong University of Science and Technology, Clear Water Bay, Kowloon, Hong Kong, 999077, P.R. China

²State Key Laboratory of Metastable Materials Science and Technology, Yanshan University, Qinhuangdao 066004, P.R. China

³Chemical Sciences and Engineering Division Argonne National Laboratory 9700 Cass Ave, Lemont, IL 60439, USA

⁴Department of Applied Physics, Research Institute for Smart Energy, The Hong Kong Polytechnic University, Hong Kong, China

⁵Materials and Process Simulation Center (MSC), MC 139-74, California Institute of Technology, Pasadena CA, 91125, USA

⁶State Key Laboratory of Heavy Oil Processing, College of Chemistry and Chemical Engineering, Institute of New Energy, China University of Petroleum (East China), Qingdao 266580 (P. R. China)

Corresponding authors email: keztluo@ust.hk, wag@caltech.edu, wuwt@upc.edu.cn, and ye.ap.zhu@polyu.edu.hk

Abstract

We demonstrate the design of graphene-supported dual atom catalysts (DACs) for the four-electron oxygen reduction reaction (ORR), by utilizing the non-bonding interaction of counterpart metals (M) that synergistically tune the electronic properties and catalytic activity of the Fe site in FeMN6-DAC and FeMN8-DAC systems, where M stands for Fe, Co, Ni, Cu, and Zn. More specifically, for Fe-M distances below 15 Å, the non-bonding interaction is significant, making the system act as the DAC. We predicted that FeNi6-DAC and FeNi8-DAC exhibit a low ORR overpotential (η^{ORR}) of 0.28 V and 0.47 V, respectively, which are at the summits of volcano plots. This low η^{ORR} originates from the high Bader charge transfer coupled with high spin density at the Fe site in both the FeNi6-DAC and FeNi8-DAC systems, which weakens the adsorption of OH* intermediate while enhancing desorption to H₂O. Guided by these density functional theory (DFT) computational results, we synthesized FeCoN8-DAC and FeNiN8-DAC along with N-doped graphene and confirmed their structures with scanning transmission electron microscopy (STEM), X-ray photoelectron spectroscopy (XPS), X-ray absorption near-edge structure (XANES), extended X-ray absorption fine structure (EXAFS), and electron spin resonance (ESR). We verify experimentally the catalytic activities and find that FeNiN8-DAC has an experimental overpotential of 0.39 V with a Tafel slope of 47 mVdec⁻¹. Based on these results, we propose a DFT-guided strategy to tune the charge transfer and spin population of the active site toward designing DACs for electrochemical ORR.

Keywords: DFT, electrocatalyst, overpotential, spin state, descriptor

1 Introduction

2 Efficient oxygen reduction reaction (ORR) is essential for such applications as proton exchange
3 membrane fuel cells (PEMFC) and Zn-air batteries to ensure rapid reaction kinetics [1]. Single
4 atom catalysts (SACs) exhibit tunable electronic structures with high electrocatalytic ORR activity
5 [2]. However, an unavoidable obstacle in the development of SACs is the scaling relationship limit.
6 According to the scaling relationship limit there is normally a linear relationship between the
7 adsorption energies of reaction intermediates (e.g., $\Delta G_{\text{OOH}^*} = \alpha \Delta G_{\text{OH}^*} + \beta$) which makes it
8 impossible to tune independently the adsorption energy of a specific intermediate [3]. By
9 introducing a second metal into SACs, leading to dual atom catalysts (DACs), the scaling
10 relationship limit can be addressed by regulating the electronic structure and spin state of the metal
11 centers towards high-performance electrochemical reactions [4]. Previous studies have devoted
12 efforts on theoretical calculations and experimental synthesis to DACs for various electrochemical
13 applications such as CO₂ reduction reaction (CO₂RR), hydrogen evolution reaction (HER), and
14 ORR [5–11]. Although the bonding interaction through orbital coupling between the two metal
15 centers is shown to be a tool useful for addressing the scaling relationship limit toward benefiting
16 electrochemical reactions [12–17], the non-bonding interactions can also strongly affect their
17 catalytic activity [18]. For example, regulating the spin state of Fe atoms has been accomplished
18 by introducing Mn, leading to higher ORR activity [19]. In addition, non-bonding interaction of
19 Ni counterpart metal on the CO₂RR activity of Fe atoms was previously reported to enhance
20 CO₂RR [20]. That is, the presence of Ni metal can deliver charges through ligands to the Fe active
21 metal to change its spin state and activity. It has been also experimentally shown that the
22 combination of Fe and Ni atoms can surpass the ORR activity of each Fe and Ni SACs because of
23 their long distance interaction [21]. It was then reported that the presence of counterpart Zn atom
24 can affect the d-orbital electron distribution of Cu active site and facilitate the stretch and cleavage

of O-O. That is to facilitate the adsorption and desorption of reaction intermediates towards ORR [22]. However, the non-bonding interaction for electrocatalysis has not previously been investigated systematically. Therefore, the effect of counterpart metals on the spin population and charge transfer from active metal site to the reaction intermediates requires a fundamental study to tune the adsorption and desorption of reaction intermediates towards enhance electrochemical reactivity.

In this work, we use DFT calculations to examine the performance of FeMN6-DAC and FeMN8-DAC, where M stands for Fe, Co, Ni, Cu, and Zn as counterpart metals, towards ORR with FeNiN6-DAC, and FeNiN8-DAC at the summits of volcano plots. We found that the non-bonding interaction of these counterpart metals can significantly modify the ORR activity of Fe sites. Based on the feature importance analysis, we introduce a new intrinsic descriptor for the rational design of DACs towards ORR.

Inspired by these theoretical calculations, FeCoN8-DAC and FeNiN8-DAC along with N-doped sample were synthesized using a two-step pyrolysis approach. Accordingly, the local atomic structure of the DACs and their local surroundings was confirmed using X-ray photoelectron spectroscopy (XPS), X-ray absorption near-edge structure (XANES), extended X-ray absorption fine structure (EXAFS), scanning transmission electron microscope (STEM), and electron energy loss spectroscopy (EELS). The ORR activity of the synthesized DACs was measured, where we find a lower overpotential and higher activity for FeNiN8-DAC, in agreement with our theoretical predictions. These results demonstrate that DFT-guided design of DACs can enable accelerated discovery of improved electrochemical activities, providing a new tool for their rational design.

Experimental section

Chemicals

An ethanol solution of 96% is obtained from the Merck Inc. of Germany. KMnO_4 , H_2SO_4 (95%), acrylamide (AM, 99%), $\text{FeCl}_3 \cdot 6\text{H}_2\text{O}$ (97%), $\text{CoCl}_2 \cdot 6\text{H}_2\text{O}$ (99%), and $\text{NiCl}_2 \cdot 6\text{H}_2\text{O}$ (98%) are all obtained from Sigma Inc. USA. Graphite (grafguard) is used with an average particle size of 350 mm. Ultrapure (18.2 M Ω) deionized water (DI) is used for washing purposes during the whole synthesis process. All chemicals mentioned above are used as received and utilized with no further treatments.

Synthesis of graphene oxide (GO)

GO is synthesized using the modified hummers method through the exfoliation and oxidation of expanded graphite sheets during thermal treatment [23]. Briefly, microwave-expanded graphite (1 g) is dispersed into 30 ml of H_2SO_4 (98%) inside a 500 ml round bottom flask, followed by stirring in an ice bath. After a duration of 2 hours, 5 g of KMnO_4 is slowly added to the suspension. Subsequently, the suspension is kept stirring at room temperature for 4 hours until the color became pale brownish. Then, the solution is slowly diluted with 50 ml of deionized (DI) water while the color change towards brown. After that, the solution is diluted with 200 ml of DI water while stirring for another 2 hours at room temperature. Finally, enough amount of H_2O_2 (30 wt.%) is added dropwise to the solution mixture to reduce the residual KMnO_4 until the solution's color is converted into bright green. The solution is stirred for another 2 hours and then allowed to settle for 1 day. The synthesized GO is then centrifuged and washed at least 9 times with DI water at 15000 rpm for 30 min. The centrifuged GO solution is ultimately reached to 8 mg/ml concentration by dispersing into DI water for further experiments.

Synthesis of DACs

Different types of catalysts supported by graphene are synthesized, namely, FeCoN8-DAC and FeNiN8-DAC, along with nitrogen-doped graphene (N-doped). Metal precursors, $\text{FeCl}_3 \cdot 6\text{H}_2\text{O}$, $\text{CoCl}_2 \cdot 6\text{H}_2\text{O}$, and $\text{NiCl}_2 \cdot 6\text{H}_2\text{O}$ salts is dissolved to make 0.05 M solution of Fe^{3+} , Co^{2+} , and Ni^{2+}

respectively [24,25]. GO suspension is diluted by mixing 12.5 ml of 8 mg/ml GO into 120 ml DI water. 125 μ l of 0.05 M of Fe^{3+} and Co^{2+} solutions and 1.2 ml of acrylamides (25 wt.%, as a nitrogen precursor) are added into the diluted GO suspension and stirred for 23 hours. The mixed solution is freeze-dried for four days and went through a two-step annealing process, as following, to synthesize highly dispersed DACs [26]. The brownish freeze-dried sample went through the first annealing step in a 1-inch quartz tube furnace at 300 $^{\circ}\text{C}$ for 3 hours under Ar (202 sccm). Then the blackish sample is washed using H_2SO_4 (0.05 M) and ethanol (96%) five times before being freeze-dried. Subsequently, the freeze-dried sample went through a second annealing process at 500 $^{\circ}\text{C}$ for 3 hours under Ar (202 sccm) to produce FeCoN8-DACs. Similarly, FeNiN8-DAC is prepared using 125 μ l of 0.05 M of each Fe^{3+} and Ni^{2+} solution as the metal precursors in the procedure mentioned above. The control sample (N-doped) is prepared without adding a metal precursor.

Characterization and analysis

The structure and morphology of synthesized DACs were examined by scanning transmission electron microscopy (STEM, JEOL JEM-2100F) combined with electron energy loss spectroscopy (EELS) and scanning electron microscopy (SEM, JEOL JSM-7800F). Chemical structure verification, elemental composition, and elemental bonding states were extracted from X-ray photoelectron spectroscopy (XPS) with a PHI 5600 (Physical Electronics). All XPS spectra were corrected concerning the C 1s peak (284.48 eV). Energy dispersive x-ray analysis (EDX, JEOL JEM 100CXII, and JEOL JSM-7800F) was used for the elemental mapping. The Fe-K, Co-K, and Ni-K edge was acquired through the synchrotron radiation-based XAFS facility at Argonne Photon Source (APS) through the X-ray Absorption Spectroscopy (XAS) to investigate the local environment around metal atoms. ATHENA, ARTEMIS, and IFEFFIT analysis tools provided in the Demeter processing package are used to analyze the obtained XAS and EXAFS data. DACs

were then analyzed using XRD (PANalytical) and Raman (Renishaw Raman RM3000 scopes with a 514 nm laser source).

Electrocatalytic activity

The ORR test was conducted via taking 5 mg of each of N-doped, FeCoN8-DAC, or FeNiN8-DAC samples, 100 μ L Nafion (5 wt.% in a mixture of lower aliphatic alcohols and water), 700 μ L of DI water and 300 ml of ethyl alcohol. The mixture was sonicated for 10 min to get a homogeneous catalyst ink. Then, 30 μ L of ink as a catalyst was loaded on a 5 mm diameter surface of the neat and clean, glassy carbon electrode (GCE). We used 5 mm diameter GCE for ORR performance, and three electrode cell was used for measurements and loaded with 0.5 M H₂SO₄ aqueous electrolyte for testing ORR. The loading for as-prepared catalyst is 0.375 mg cm⁻². The Ag/AgCl was used as a reference electrode which was prior filled in saturated KCl, while glassy carbon was used as a working electrode and Pt wire as a counter electrode. RHE potential was used via $E_{\text{RHE}} = E_{\text{Ag/AgCl}} + 0.197 + 0.0592 \times \text{pH}$. Highly pure Ar (99.99%) and O₂ (99.99%) were purged to H₂SO₄ electrolyte for 30 min before testing our catalysts and measured the CV with a scan rate of 50 mVs⁻¹.

From positive to negative, the rotating speed (400, 800, 1200, 1600, and 2000 rpm) was used to measure the LSV polarization curve with the rate of sweeping at 10 mV/s. Tafel slopes for ORR was obtained from corresponding LSV curves. The ORR Tafel slope for all catalysts is drawn against logarithmic scale current density versus working potential; all catalysts' ORR Tafel slope was determined. The ORR polarization curves of the FeNiN8-DACs were also carried out at different rotation speed (400 rpm-2000rpm) to obtain Koutecky-Levich (K-L) plot based on the following equation [25]:

$$\frac{1}{j} = \frac{1}{B\omega^{1/2}} + \frac{1}{j_K} \quad (1)$$

$$B = 0.2nFC_0(D_0)^{2/3}\nu^{-1/6} \quad \text{and} \quad j_K = nFkC_0 \quad (2)$$

Where j is the measured current density, ω is the electrode rotation rate, F is the Faraday constant, C_0 is the bulk concentration of O_2 , D_0 is the diffusion coefficient of O_2 , ν is the kinetic viscosity of the electrolyte.

DFT calculations

The atomic and electronic structures of DACs were computed using first-principles density functional theory (DFT) in Gaussian 09 software. Theoretical calculations were performed at the Becke, 3-parameter, Lee–Yang–Parr (B3LYP) exchange functional level of DFT along with 6-31G (d, p) basis set for the geometry optimizations. Also, the DFT-D3 method was used to include van der Waals interactions. We used the solvation model density (SMD) as a universal continuum solvation model to include solvent effects (H_2O) [27]. The effect of magnetic coupling was considered in all the DFT calculations [13]. Electron density and projected density-of-states (DOS) were generated with the Multiwfn 3.8 program [28]. We calculated the vibrational frequencies to obtain Gibbs free energies for analyzing the ORR reaction mechanism. According to previous studies the Fe atom is the active site for ORR, so only the Fe based sites were considered for this study [29].

Results and discussion

First, we calculated the Gibbs free energy profiles of FeMN8-DAC and FeMN6-DAC (M: Fe, Co, Ni, Cu, and Zn) for ORR. **Scheme1a** shows the structure of FeMN6-DAC and FeMN8-DAC with Fe-M distances of 7.58 Å and 2.58 Å, respectively. The distances are measured based on the optimized structure without any adsorbate. The green semi circles indicate the non-bonding effect of M counterpart metals which can deliver charges through the intervening ligands to the Fe active

1 metal to modify its spin state and ORR activity. **Scheme1b** indicates the lateral view of ORR
 2 intermediates, indicating the spin-crossover of Fe site during ORR. In fact, the interaction between
 3 the π^* orbital of the reaction intermediates and the d orbitals of Fe site leads to changes in both the
 4 d-orbital splitting and the delocalization of electrons from low-lying d_{xy} and d_{yz} orbitals to the
 5 high-lying $d_{x^2-y^2}$ orbital of Fe [30]. As shown in **Scheme 1b**, the ORR may proceed through the
 6 following fundamental steps, which are normally used to investigate electrocatalysis of the ORR
 7 on the Fe active site [31]:



8 Because it is difficult to obtain the exact free energy of OOH, O, OH, and H radicals in the
 9 electrolyte solution, the Gibbs free energies of ΔG_{OOH^*} , ΔG_{O^*} , ΔG_{OH^*} , and ΔG_{H^*} are relative to the
 10 free energy of stoichiometrically appropriate amounts of H_2O (g) and H_2 (g), defined as follows
 11 [31]:

$$\Delta G_{\text{OH}^*} = E_{\text{DAC-OH}^*} - E_{\text{DAC}} + \frac{1}{2}E_{\text{H}_2} - E_{\text{H}_2\text{O}} + \Delta\text{ZPE} - T\Delta S \quad (7)$$

$$\Delta G_{\text{O}^*} = E_{\text{DAC-O}^*} - E_{\text{DAC}} + E_{\text{H}_2} - E_{\text{H}_2\text{O}} + \Delta\text{ZPE} - T\Delta S \quad (8)$$

$$\Delta G_{\text{OOH}^*} = E_{\text{DAC-OOH}^*} - E_{\text{DAC}} + \frac{3}{2}E_{\text{H}_2} - 2E_{\text{H}_2\text{O}} + \Delta\text{ZPE} - T\Delta S \quad (9)$$

$$\Delta G_{\text{O}_2^*} = E_{\text{DAC-O}_2^*} - E_{\text{DAC}} + 2E_{\text{H}_2} - 2E_{\text{H}_2\text{O}} + \Delta\text{ZPE} - T\Delta S \quad (10)$$

12 E_{H_2} and $E_{\text{H}_2\text{O}}$ represent the energy of gas phase H_2 and H_2O , respectively. $E_{\text{DACs-H}^*}$, $E_{\text{DACs-OH}^*}$,
 13 $E_{\text{DACs-O}^*}$, and $E_{\text{DACs-OOH}^*}$ are the total energy of **DACs** with adsorbed H, OH, O, and OOH states,

1 respectively. E_{DACs} is the energy of DAC surface, ΔZPE is zero-point energy (ZPE) correction,
 2 $T\Delta S$ is entropy correction, and T is the temperature.

3 The adsorption free energies of ORR are approximately independent of the pH of the solution [29].
 4 The difference between the equilibrium potential of $U=1.23$ V and the limiting potential is the
 5 theoretical ORR overpotential (η^{ORR}), and limiting potential is the highest potential at which all
 6 the reaction steps are downhill in free energy (see section S2 of Supporting Information) [32]. The
 7 reaction step which is flat in free energy at the limiting potential is the rate determining step [32].

8 **Figure 1a** illustrates the Gibbs free energies diagram of reaction intermediates for FeNiN6-DAC
 9 (see **Figure S10-S12** for other FeMN6-DAC and FeMN8-DAC). **Figure 1a** shows that the
 10 formation of H_2O from OH^* is the ORR rate-determining step, because this reaction step, which
 11 is shown as a blue dashed circle, is flat in free energy at the limiting potential of 0.95. From **Figure**
 12 **1a**, we find that the ORR limiting potential and η^{ORR} of FeNiN6-DAC are 0.95 V and $|1.23-$
 13 $0.95|=0.28$ V, respectively. **Figure 1b** shows the volcano plot of theoretical η^{ORR} , obtained from
 14 **Figure S10-S12**, versus the number of d electrons of the counterpart metal (M). We found that
 15 FeNiN6-DAC and FeNiN8-DAC are both at the summit with the η^{ORR} of 0.28 V and 0.47 V,
 16 respectively, which are comparable with theoretically obtained η^{ORR} of 0.43 V for the benchmark
 17 Pt(111) [31], 0.33 V for CoRu@N8V4 [33], and 0.34 for CoCuN6-gra(OH) [13]. In contrast, the
 18 FeCuN8-DAC and FeZnN8-DAC possess unfavorable theoretical η^{ORR} of 0.68 V and 0.83 V,
 19 respectively. **Figure S16** displays the counter plot of η^{ORR} versus the d electrons of M and Fe-M
 20 distance ($D_{\text{Fe-M}}$), suggesting that the ORR overpotential increases with the Fe-M distance. Our
 21 evaluation on the DAC systems revealed that for $D_{\text{Fe-M}} < 15$ Å, the system acts as a DAC, while for
 22 $D_{\text{Fe-M}} > 15$ Å, the M atom has no significant impact on the catalytic activity of active site, so the
 23 system acts as a SAC.

To shed more light on the effect of counterpart M metals on the ORR activity of Fe site, we plotted the projected density of states (PDOS) for the Fe sites. **Figure 1c** shows the PDOS of 3d orbitals at the Fe site in FeNiN6-DAC before and after interaction with OH*. Some peaks disappeared and other peaks evolved after interacting with OH*. The new peaks are designated as bonding (σ) and antibonding (σ^*) orbitals, indicating the interaction of the Fe site with OH* [24]. **Figure S13** shows the PDOS of 3d orbitals of Fe site for FeNiN6-DAC and FeN4-SAC systems, indicating that the active valence 3d_{z2} orbital of the Fe in FeNiN6-DAC shifted down, weakening the interaction with reaction intermediates. Thus, the reaction activity of Fe site in FeMN6-DAC and FeMN8-DAC structures strongly depends on the non-bonding interaction between Fe and the counterpart metals (M).

According to **Figure 1b** and **Figure S16**, our results show that the ORR catalytic activity of Fe metal depends strongly on the number of d electrons of counterpart metal (M). This agrees with the feature importance analysis performed using the machine learning (ML) [34,35] technique on the Gibbs free energy of ORR intermediates, which suggested that the electronegativity and d electron numbers of the counterpart M metal as the most important parameters (**Figure S32**). Inspired by the feature importance analysis shown in **Figure S32**, a simple descriptor (φ) is introduced to consider the effect of most important parameters describing the ORR activity of DACs:

$$\varphi = \frac{|\theta_{d,M} - 1.33\theta_{d,Fe}|}{E_M} - \frac{D_0}{D_{Fe-M}} \quad (11)$$

θ_d is the number of d orbital valence electrons of M, E_M is the electronegativity of M, D_0 is the closest distance between Fe and M metals (2.58 Å), and D_{Fe-M} is the distance between Fe and M metals (between $D_0=2.58$ Å and 15 Å). As shown in **Figure 1d**, η^{ORR} increases linearly with the

descriptor ϕ . Similarly, as shown in **Figure S28**, the new descriptor satisfactory defines the η^{ORR} , Gibbs free energy of reaction intermediates and spin population of Fe site.

As shown in **Table S2**, the Mulliken charge of Fe is 1.238, 1.332, 1.321, 1.253, 1.193, 1.264, 1.311, 1.302, 1.269, and 1.283 e^- , respectively, for FeFeN8-DAC, FeCoN8-DAC, FeNiN8-DAC, FeCuN8-DAC, FeZnN8-DAC, FeFeN6-DAC, FeCoN6-DAC, FeNiN6-DAC, FeCuN6-DAC, and FeZnN6-DAC. As shown in **Figure S17**, a specific charge is transferred from Fe atom to the

counterpart metals (M) which depends directly on the electronegativity of the counterpart M atom.

Thus, a relatively high charge is transferred from Fe to Ni site (**Figure S18**) [36], increasing the oxidation state of Fe site, weakening the adsorption of *OH intermediate [37,38], and decreasing the ORR overpotential [39] by increasing the spin density of Fe site (**Figure 2a**). These results are

in great agreement with the electron spin resonance (ESR) spectroscopy results for N-doped, FeCoN8-DAC, and FeNiN8-DAC at 77 K, which are shown in **Figure 2b**. The g values of around 2.00 in the ESR spectra are assigned to the unpaired electron in the $3d_{z^2}$ and $3d_{x^2-y^2}$ orbitals of Fe^{2+}

[40]. The ESR spectrum for FeNiN8-DAC indicates a stronger signal than FeCoN8-DAC, while this signal disappears in N-doped graphene, suggesting additional unpaired 3d electrons for Fe in the FeNiN8-DAC system [19,41,42]. In addition, **Figure 2c** shows high charge transfer between FeNiN6-DAC and the OH^* intermediate, in agreement with recent work [43]. **Figures 2d-e**

indicates high spin polulation of Fe site in FeNiN6-DAC and yet its high charge transfer, facilitates OH^* desorption to release H_2O , which makes this configuration a promising catalyst for ORR [22,44].

Based on the above calculations, we synthesized FeCoN8-DAC and FeNiN8-DAC along with N-doped graphene samples. The chemical states and compositions of the prepared samples were studied with X-ray photoelectron spectroscopy (XPS). The XPS results show the Fe and Co metal

contents to be 0.20 and 0.18 wt.% respectively, in the FeCoN8-DAC sample. The Fe and Ni metal contents are 0.19 and 0.18 wt.% respectively, in the FeNiN8-DAC sample. This suggests an Fe/Ni and Fe/Co molar ratios of around 1:1. To identify different types of nitrogen in the DACs, we deconvoluted the N 1s peak, suggesting different types of nitrogen for FeNiN8-DAC, and N-doped samples. For example, **Figure S1b** shows that the N 1s peak for FeNiN8-DAC deconvoluted into pyridinic-N (398.1 eV), Fe-N (398.7 eV), pyrrolic-N (400.1 eV), and oxidized-N (406.9 eV) [24]. **Figure 3a-c** shows a high-resolution peak spectrum for Fe, Co, and Ni metals of the synthesized samples, indicating two valence states ($p_{1/2}$ and $p_{3/2}$) for Fe, Co, and Ni with the partially oxidative states [20,29]. The binding energy of Fe $2p_{3/2}$ in FeNiN8-DAC shifts by +0.1 eV compared with that in FeCoN8-DAC, suggesting a lower valence state for Fe [20]. This is in agreement with the Mulliken charge analysis of Fe, changing from 1.332 e^- to 1.104 e^- , respectively, for FeCoN8-DAC and FeNiN8-DAC, suggesting that the Ni atom donates fewer electrons to Fe atom than does Co [45].

The electronic states and atomic configuration of the metal atoms in the synthesized samples were further investigated with the XANES and EXAFS. **Figure 3d-f** show the metal K-edge XANES spectra for FeCoN8-DAC and FeNiN8-DAC, indicating that the local atomic structure around Fe, Co, and Ni metal atoms is distinct from their bulk metals. **Figure 3d-f** indicates a blue-shift in the absorption edge of these metals compared to their bulk sample, suggesting a valence state higher than 0. We attribute the higher valence state to coordination between the metals and the N8 coordination [24,25,40]. Moreover, three peaks for Fe atom in **Figure 3d** indicate to $1s \rightarrow 3d$, $1s \rightarrow 4p_z$, and $1s \rightarrow 4p_{xy}$ transitions [40]. The differences in intensity of peak C as the main edge peak in **Figure 3d1** is confirmed by the existence of divacancy-based M-N₄C₄ moieties bonded axially with broken D_{4h} symmetry [24]. In addition, we observe a downshift in the main peak C

of the K-edge XANES spectra of FeNiN8-DAC compared to FeCoN8-DAC, suggesting delocalization of unpaired electrons in the high-lying d_{z^2} orbital of Fe onto ligands [30], more clearly shown through the spin density in **Figure S14**. In addition, as shown in the inset of **Figure 3a**, the Fe K-edge XANES spectra of FeCoN8-DAC shows a red-shift in the adsorption edge compared to FeNiN8-DAC, indicating a decreased valence of Fe in FeCoN8-DAC [45], in agreement with the XPS results. The red-shift in the Fe K-edge XANES spectra can be obtained from theory using the accurate finite difference (FD) approach implemented in the FDMNES software [24,46], shown in **Figure S33**.

In addition, the bonding and coordination environment around the metal in the DACs were further studied using EXAFS Fourier transform (FT) for FeCoN8-DAC and FeNiN8-DAC. **Figure 3g-i** shows that the EXAFS FT spectra of FeCoN8-DAC and FeNiN8-DAC exhibit primary peaks corresponding to Fe-N bonding at around 1.42 Å, different from the Fe-O peak at 1.55 Å [29] and Fe-Fe peaks at 2.17 and 4.48 Å. The EXAFS FT spectra for the FeCoN8-DAC sample exhibits a primary peak attributed to Co-N at 1.40 Å, different from the Co-O peak at 1.63 Å [47] and Co-Co peaks at 2.15 and 4.20 Å. Similarly, the EXAFS FT spectra for the FeNiN8-DAC sample exhibits a primary peak attributed to Ni-N bonding at 1.43 Å, different from the Ni-O peak at 1.62 Å [47] and Ni-Ni peaks at 2.17 and 4.19 Å. These results confirm that the coordination environment around the metal atoms corresponding to metal-N interaction.

Figure 4a and 4c shows the STEM images of FeCoN8-DAC and FeNiN8-DAC samples, respectively, where the individual metal atoms (white dots) distribute homogeneously throughout the whole graphene support. EELS analysis on the specimen confirms that the brighter dots are Co/Fe atoms in the FeCoN8-DAC sample and Fe/Ni atoms in the FeNiN8-DAC sample, as shown in **Figure 4b and 4d**, respectively. The surface structure, morphology, and elemental mapping of

FeCoN8-DAC and FeNiN8-DAC are confirmed by SEM images (**Figure S2**). **Figures S3** and **S4** show the SEM imaging and EDX elemental mapping for Fe, C, N, Co, and Ni elements, confirming the uniform presence of all elements. **Figure S5b** also shows the TEM image for the FeNiN8-DAC sample, suggesting the uniform dispersion of the Fe and Ni metal atoms without noticeable aggregation. The results are consistent with an XRD spectrum provided in **Figure S6** for N-doped, FeCoN8-DAC, and FeNiN8-DAC samples. The XRD spectra occupy only one broad graphitic carbon peak (002) at 23.3° . No other peak is detected that would correspond to metal species or their compounds with oxides or nitrides [24]. **Figure S5a** displays the STEM image for the FeNiN8-DAC sample, suggesting the rich porous support, which is in consistent with a Raman spectrum provided in **Figure S7**. As shown in **Figure S7**, the intensity ratio of D/G-band (I_D/I_G) in the Raman spectra increases from 0.760 to 0.868 and the density of defect vacancies (ρ_D) increases from 2.30 nm^{-2} to 2.63 nm^{-2} for graphene oxide (GO) and FeNiN8-DAC sample, respectively (see Supporting Information for more details) [48].

The ORR performance of all synthesized materials was checked, including rotating disk electrode tests in acidic medium, 0.5 M H_2SO_4 . As shown in **Figure 5a**, the reduction current appears at +0.84 V versus RHE for the FeNiN8-DAC sample, corresponding to a very low overpotential of $1.23 - 0.84 = 0.39 \text{ V}$, which is comparable to our theory obtained overpotential of 0.47 V, **Figure 1b**. However, for FeCoN8-DAC and N-doped the onset potential was more negative than FeNiN8-DAC. The as-synthesized DACs are judged through Tafel slope values resulting from corresponding ORR curves shown in **Figure S9**. Out of all samples, the FeNiN8-DAC sample delivered the lowest Tafel slope of 47 mVdec^{-1} , comparable with 60 mVdec^{-1} obtained for Fe/Ni-Nx/OC [49]. This value is significantly lower than the Tafel slope values of FeCoN8-DAC (65 mVdec^{-1}) and N-doped graphene (64 mVdec^{-1}), suggesting that the FeNiN8-DAC has favorable

reaction kinetics for ORR applications. This agrees with our DFT results in **Figure 1b**, showing that FeNiN8-DAC has a lower overpotential than FeCoN8-DAC. Cyclic voltammetry (CV) measurements of FeNiN8-DAC were carried out in 0.5 M H₂SO₄ acidic solution at a scan rate of 50 mVs⁻¹ under saturated O₂ and Ar, as shown in **Figure 5b**. The CV curve of FeNiN8-DAC under O₂ revealed a prominent ORR peak (red line) at 0.72 V versus RHE, while the corresponding peak is absent under Ar-saturated electrolyte (black line). This shows that O₂ is reduced by FeNiN8-DAC. **Figure 5c** displays the ORR polarization curves of the FeNiN8-DAC with various rotation speeds of 400 to 2000 rpm, indicating higher reaction rates for higher rotation speeds. The K-L plots for the applied potentials of 0.30, 0.35, and 0.40 V are shown in **Figure 5d**, indicating good linearity for all applied potentials. $B = 0.15$ in equation 2 is determined from the slope of the K-L equation and the ORR kinetic current density, $j_K = 22.5 \text{ mAcm}^{-2}$, is calculated from the K-L plot, which is comparable to $j_K = 28.1 \text{ mAcm}^{-2}$ obtained for Fe/Ni-Nx/OC [49], suggesting a proficient electron transfer process. Besides, a cycling stability test was carried out to investigate the long-lasting durability of the FeNiN8-DAC in O₂-saturated electrolytes. As shown in **Figure S8**, after 550 cycles at the scan rate of 2000 mVs⁻¹ and the potential window between 0 and 1.5 V (versus RHE), the FeNiN8-DAC possesses its original onset potential, while the current density decreased a little, indicating its satisfactory stability.

Conclusion

We demonstrate the design of graphene-supported dual atom catalysts (DACs) for four-electron oxygen reduction reaction (ORR) using density functional theory (DFT) calculations validated with experiments. We observed that the non-bonding interaction of counterpart metals (M: Fe, Co, Ni, Cu, and Zn) plays an important role in lowering the ORR overpotential of Fe sites in FeMN6-DAC and FeMN8-DAC structures. More specifically, FeNiN6-DAC and FeNiN8-DAC exhibit

low ORR overpotentials of 0.28 V and 0.47 V, respectively, as compared with 0.71 V for FeN₄-SAC. In addition, based on the feature importance analysis, we introduce a new intrinsic descriptor to describe the properties of these DACs towards ORR. Guided by these computational results, we synthesized FeCoN₈-DAC and FeNiN₈-DAC along with N-doped graphene and confirmed their structures with scanning transmission electron microscopy (STEM), X-ray photoelectron spectroscopy (XPS), X-ray absorption near-edge structure (XANES), and extended X-ray absorption fine structure (EXAFS). Subsequently, we measured the catalytic activity of FeCoN₈-DAC and FeNiN₈-DAC for ORR. We found that FeNiN₈-DAC demonstrates a higher catalytic activity with overpotential of 0.47 V, comparable to 0.43 V for the benchmark Pt/C. Based on these results, we propose a DFT-guided strategy for designing FeMN₆-DAC and FeMN₈-DAC for electrochemical ORR.

Acknowledgements

Z.L. acknowledge supports by RGC (16304421), and the IER foundation (HT-JD-CXY-201907), “International science and technology cooperation projects” of Science and Technological Bureau of Guangzhou Huangpu District (2019GH06), Guangdong Science and Technology Department (Project#:2020A0505090003), Research Fund of Guangdong-Hong Kong-Macao Joint Laboratory for Intelligent Micro-Nano Optoelectronic Technology (No. 2020B1212030010). Technical assistance from the Materials Characterization and Preparation Facilities of HKUST is greatly appreciated. Q.P. thanks the Natural Science Foundation of Hebei Province for Innovation Groups Program (C2022203003). WAG thanks the US National Science Foundation (CBET-2005250) for support. Y.Z. thanks the financial support from the Hong Kong Polytechnic University (Grant No. ZVRP).

Associated Content

Supporting Information

Characterization, DFT calculations, Descriptor, and Machine Learning (ML) on Gibbs free energy.

1 **Conflicts of interest**

2 These authors respectfully declare that there are no conflicts of interest to acknowledge for this
3 research.

4

5

References

- [1] X. Li, Z. Xiang, Identifying the impact of the covalent-bonded carbon matrix to FeN₄ sites for acidic oxygen reduction, *Nat. Commun.* 13 (2022).
<https://doi.org/10.1038/s41467-021-27735-1>.
- [2] Y. Wu, Q. Wu, Q. Zhang, Z. Lou, K. Liu, Y. Ma, Z. Wang, Z. Zheng, H. Cheng, Y. Liu, Y. Dai, B. Huang, P. Wang, An organometal halide perovskite supported Pt single-atom photocatalyst for H₂ evolution, *Energy Environ. Sci.* 15 (2022) 1271–1281.
<https://doi.org/10.1039/d1ee03679c>.
- [3] L. Li, K. Yuan, Y. Chen, Breaking the Scaling Relationship Limit: From Single-Atom to Dual-Atom Catalysts, *Accounts Mater. Res.* (2021).
<https://doi.org/10.1021/accountsmr.1c00264>.
- [4] F. Rehman, S. Kwon, C.B. Musgrave, M. Tamtaji, W.A. Goddard, Z. Luo, High-throughput screening to predict highly active dual-atom catalysts for electrocatalytic reduction of nitrate to ammonia, *Nano Energy.* 103 (2022) 107866.
<https://doi.org/10.1016/j.nanoen.2022.107866>.
- [5] J. Wang, Z. Huang, W. Liu, C. Chang, H. Tang, Z. Li, W. Chen, C. Jia, T. Yao, S. Wei, Y. Wu, Y. Li, Design of N-Coordinated Dual-Metal Sites: A Stable and Active Pt-Free Catalyst for Acidic Oxygen Reduction Reaction, *J. Am. Chem. Soc.* 139 (2017) 17281–17284. <https://doi.org/10.1021/jacs.7b10385>.
- [6] M. Feng, X. Wu, H. Cheng, Z. Fan, X. Li, F. Cui, S. Fan, Y. Dai, G. Lei, G. He, Well-defined Fe-Cu diatomic sites for efficient catalysis of CO₂ electroreduction, *J. Mater. Chem. A.* 9 (2021) 23817–23827. <https://doi.org/10.1039/d1ta02833b>.
- [7] Z. Zeng, L.Y. Gan, H. Bin Yang, X. Su, J. Gao, W. Liu, H. Matsumoto, J. Gong, J. Zhang, W. Cai, Z. Zhang, Y. Yan, B. Liu, P. Chen, Orbital coupling of hetero-diatom nickel-iron site for bifunctional electrocatalysis of CO₂ reduction and oxygen evolution, *Nat. Commun.* 12 (2021) 1–11. <https://doi.org/10.1038/s41467-021-24052-5>.
- [8] N. Karmodak, S. Vijay, G. Kastlunger, K. Chan, Computational Screening of Single and Di-Atom Catalysts for Electrochemical CO₂ Reduction, *ACS Catal.* (2022) 4818–4824.

<https://doi.org/10.1021/acscatal.1c05750>.

- [9] Y. Cheng, S. He, J.P. Veder, R. De Marco, S. ze Yang, S. Ping Jiang, Atomically Dispersed Bimetallic FeNi Catalysts as Highly Efficient Bifunctional Catalysts for Reversible Oxygen Evolution and Oxygen Reduction Reactions, *ChemElectroChem*. 6 (2019) 3478–3487. <https://doi.org/10.1002/celec.201900483>.
- [10] Z. Xiao, P. Sun, Z. Qiao, K. Qiao, H. Xu, S. Wang, D. Cao, Atomically dispersed Fe-Cu dual-site catalysts synergistically boosting oxygen reduction for hydrogen fuel cells, *Chem. Eng. J.* 446 (2022) 137112. <https://doi.org/10.1016/j.cej.2022.137112>.
- [11] Y. Ma, H. Fan, C. Wu, M. Zhang, J. Yu, L. Song, K. Li, J. He, An efficient dual-metal single-atom catalyst for bifunctional catalysis in zinc-air batteries, *Carbon N. Y.* 185 (2021) 526–535. <https://doi.org/10.1016/j.carbon.2021.09.044>.
- [12] Y. Wang, B.J. Park, V.K. Paidi, R. Huang, Y. Lee, K.J. Noh, K.S. Lee, J.W. Han, Precisely Constructing Orbital Coupling-Modulated Dual-Atom Fe Pair Sites for Synergistic CO₂ Electroreduction, *ACS Energy Lett.* 7 (2022) 640–649. <https://doi.org/10.1021/acsenenergylett.1c02446>.
- [13] L. Yu, F. Li, J. Zhao, Z. Chen, Revisiting catalytic performance of supported metal dimers for oxygen reduction reaction via magnetic coupling from first principles, *Adv. Powder Mater.* 1 (2022) 100031. <https://doi.org/10.1016/j.apmate.2022.01.004>.
- [14] F. Kong, R. Si, N. Chen, Q. Wang, J. Li, G. Yin, M. Gu, J. Wang, L.M. Liu, X. Sun, Origin of hetero-nuclear Au-Co dual atoms for efficient acidic oxygen reduction, *Appl. Catal. B Environ.* 301 (2022) 120782. <https://doi.org/10.1016/j.apcatb.2021.120782>.
- [15] Y. Li, B. Wei, M. Zhu, J. Chen, Q. Jiang, B. Yang, Y. Hou, L. Lei, Z. Li, R. Zhang, Y. Lu, Synergistic Effect of Atomically Dispersed Ni–Zn Pair Sites for Enhanced CO₂ Electroreduction, *Adv. Mater.* 33 (2021) 1–12. <https://doi.org/10.1002/adma.202102212>.
- [16] T. He, B. Yu, Y. Zhang, X. Ouyang, S. Chen, Rational design of carbon-supported single and dual atom catalysts for bifunctional oxygen electrocatalysis, *Curr. Opin. Electrochem.* (2022) 101197.
- [17] T. He, A.R.P. Santiago, Y. Kong, M.A. Ahsan, R. Luque, A. Du, H. Pan, Atomically

- Dispersed Heteronuclear Dual-Atom Catalysts: A New Rising Star in Atomic Catalysis, *Small*. 2106091 (2021). <https://doi.org/10.1002/sml.202106091>.
- [18] W. Li, J. Yang, D. Wang, Long-Range Interactions in Diatomic Catalysts Boosting Electrocatalysis, *Angew. Chemie*. 202213318 (2022). <https://doi.org/10.1002/ange.202213318>.
- [19] G. Yang, J. Zhu, P. Yuan, Y. Hu, G. Qu, B.A. Lu, X. Xue, H. Yin, W. Cheng, J. Cheng, W. Xu, J. Li, J. Hu, S. Mu, J.N. Zhang, Regulating Fe-spin state by atomically dispersed Mn-N in Fe-N-C catalysts with high oxygen reduction activity, *Nat. Commun.* 12 (2021) 4–13. <https://doi.org/10.1038/s41467-021-21919-5>.
- [20] L. Jiao, J. Zhu, Y. Zhang, W. Yang, S. Zhou, A. Li, C. Xie, X. Zheng, W. Zhou, S.H. Yu, H.L. Jiang, Non-Bonding Interaction of Neighboring Fe and Ni Single-Atom Pairs on MOF-Derived N-Doped Carbon for Enhanced CO₂ Electrocatalytic Reduction, *J. Am. Chem. Soc.* 143 (2021) 19417–19424. <https://doi.org/10.1021/jacs.1c08050>.
- [21] J. Zhao, L. Zong, L. Cui, F. Lu, Z. Xiao, L. Wang, Synthesis of Dual-metal Single Atom in Porous Carbon Nanospheres with Enhanced Oxygen Reduction Activity in Both Acidic and Alkaline Electrolytes, *J. Colloid Interface Sci.* (2022). <https://doi.org/10.1016/j.jcis.2022.11.147>.
- [22] M. Tong, F. Sun, Y. Xie, Y. Wang, Y. Yang, C. Tian, L. Wang, H. Fu, Operando Cooperated Catalytic Mechanism of Atomically Dispersed Cu–N₄ and Zn–N₄ for Promoting Oxygen Reduction Reaction, *Angew. Chemie - Int. Ed.* 60 (2021) 14005–14012. <https://doi.org/10.1002/anie.202102053>.
- [23] W.S. Hummers, R.E. Offeman, Preparation of Graphitic Oxide, *J. Am. Chem. Soc.* 80 (1958) 1339. <https://doi.org/10.1021/ja01539a017>.
- [24] M.D. Hossain, Z. Liu, M. Zhuang, X. Yan, G.L. Xu, C.A. Gadre, A. Tyagi, I.H. Abidi, C.J. Sun, H. Wong, A. Guda, Y. Hao, X. Pan, K. Amine, Z. Luo, Rational Design of Graphene-Supported Single Atom Catalysts for Hydrogen Evolution Reaction, *Adv. Energy Mater.* 9 (2019). <https://doi.org/10.1002/aenm.201803689>.
- [25] K. Khan, T. Liu, M. Arif, X. Yan, M.D. Hossain, F. Rehman, S. Zhou, J. Yang, C. Sun,

- 1 S.H. Bae, J. Kim, K. Amine, X. Pan, Z. Luo, Laser-Irradiated Holey Graphene-Supported
2 Single-Atom Catalyst towards Hydrogen Evolution and Oxygen Reduction, *Adv. Energy*
3 *Mater.* 2101619 (2021) 1–9. <https://doi.org/10.1002/aenm.202101619>.
- 4 [26] X. Hai, S. Xi, S. Mitchell, K. Harrath, H. Xu, D.F. Akl, D. Kong, J. Li, Z. Li, T. Sun, H.
5 Yang, Y. Cui, C. Su, X. Zhao, J. Li, J. Pérez-ramírez, J. Lu, Scalable two-step annealing
6 method for preparing ultra-high-density single-atom catalyst libraries, (n.d.).
7 <https://doi.org/10.1038/s41565-021-01022-y>.
- 8 [27] A. V. Marenich, C.J. Cramer, D.G. Truhlar, Universal solvation model based on solute
9 electron density and on a continuum model of the solvent defined by the bulk dielectric
10 constant and atomic surface tensions, *J. Phys. Chem. B.* 113 (2009) 6378–6396.
11 <https://doi.org/10.1021/jp810292n>.
- 12 [28] T. Lu, F. Chen, Multiwfn: A multifunctional wavefunction analyzer, *J. Comput. Chem.* 33
13 (2012) 580–592. <https://doi.org/10.1002/jcc.22885>.
- 14 [29] K. Khan, X. Yan, Q. Yu, S.H. Bae, J.J. White, J. Liu, T. Liu, C. Sun, J. Kim, H.M. Cheng,
15 Y. Wang, B. Liu, K. Amine, X. Pan, Z. Luo, Stone-Wales defect-rich carbon-supported
16 dual-metal single atom sites for Zn-air batteries, *Nano Energy.* 90 (2021) 106488.
17 <https://doi.org/10.1016/j.nanoen.2021.106488>.
- 18 [30] X. Li, C.S. Cao, S.F. Hung, Y.R. Lu, W. Cai, A.I. Rykov, S. Miao, S. Xi, H. Yang, Z. Hu,
19 J. Wang, J. Zhao, E.E. Alp, W. Xu, T.S. Chan, H. Chen, Q. Xiong, H. Xiao, Y. Huang, J.
20 Li, T. Zhang, B. Liu, Identification of the Electronic and Structural Dynamics of Catalytic
21 Centers in Single-Fe-Atom Material, *Chem.* 6 (2020) 3440–3454.
22 <https://doi.org/10.1016/j.chempr.2020.10.027>.
- 23 [31] H. Xu, D. Cheng, D. Cao, X.C. Zeng, A universal principle for a rational design of single-
24 atom electrocatalysts, *Nat. Catal.* 1 (2018) 339–348. [https://doi.org/10.1038/s41929-018-](https://doi.org/10.1038/s41929-018-0063-z)
25 [0063-z](https://doi.org/10.1038/s41929-018-0063-z).
- 26 [32] A. Kulkarni, S. Siahrostami, A. Patel, J.K. Nørskov, Understanding Catalytic Activity
27 Trends in the Oxygen Reduction Reaction, *Chem. Rev.* 118 (2018) 2302–2312.
28 <https://doi.org/10.1021/acs.chemrev.7b00488>.

- [33] J. Zhang, A. Yu, C. Sun, Computational Exploration of Dual Atom Catalysts Loaded on Defective Graphene for Oxygen Reduction Reaction, *Appl. Surf. Sci.* (2022) 154534. <https://doi.org/10.1016/j.apsusc.2022.154534>.
- [34] G. Di Liberto, S. Tosoni, L.A. Cipriano, G. Pacchioni, A Few Questions about Single-Atom Catalysts : When Modeling Helps, (2022). <https://doi.org/10.1021/accountsmr.2c00118>.
- [35] Y. Ying, K. Fan, X. Luo, J. Qiao, H. Huang, Unravelling the origin of bifunctional OER/ORR activity for single-atom catalysts supported on C₂N by DFT and machine learning , *J. Mater. Chem. A.* (2021) 16860–16867. <https://doi.org/10.1039/d1ta04256d>.
- [36] Y. Zhang, Y. Cheng, X. Wang, Q. Sun, X. He, H. Ji, Enhanced Hydrogenation Properties of Pd Single Atom Catalysts with Atomically Dispersed Ba Sites as Electronic Promoters, *ACS Catal.* (2022) 15091–15096. <https://doi.org/10.1021/acscatal.2c04626>.
- [37] S. Chen, T. Luo, X. Li, K. Chen, J. Fu, K. Liu, C. Cai, Q. Wang, H. Li, Y. Chen, C. Ma, L. Zhu, Y. Lu, T. Chan, M. Zhu, E. Cort, M. Liu, Identification of the Highly Active Co – N₄ Coordination Motif for Selective Oxygen Reduction to Hydrogen Peroxide, (2022). <https://doi.org/10.1021/jacs.2c01194>.
- [38] M. Zhang, H. Li, J. Chen, F. Ma, L. Zhen, Z. Wen, C. Xu, Transition Metal (Co , Ni , Fe , Cu) Single-Atom Catalysts Anchored on 3D Nitrogen-Doped Porous Carbon Nanosheets as Efficient Oxygen Reduction Electrocatalysts for Zn – Air Battery, 2202476 (2022) 1–10. <https://doi.org/10.1002/smll.202202476>.
- [39] C. Zhang, Y. Dai, Q. Sun, C. Ye, R. Lu, Y. Zhou, Y. Zhao, Strategy to weaken the oxygen adsorption on single-atom catalysts towards oxygen-involved reactions, *Mater. Today Adv.* 16 (2022) 100280. <https://doi.org/10.1016/j.mtadv.2022.100280>.
- [40] H. Bin Yang, S.F. Hung, S. Liu, K. Yuan, S. Miao, L. Zhang, X. Huang, H.Y. Wang, W. Cai, R. Chen, J. Gao, X. Yang, W. Chen, Y. Huang, H.M. Chen, C.M. Li, T. Zhang, B. Liu, Atomically dispersed Ni(i) as the active site for electrochemical CO₂ reduction, *Nat. Energy.* 3 (2018) 140–147. <https://doi.org/10.1038/s41560-017-0078-8>.
- [41] X. Wang, Y. Fu, D. Tranca, K. Jiang, J. Zhu, J. Zhang, S. Han, C. Ke, C. Lu, X. Zhuang,

Regulating the Spin State of Nickel in Molecular Catalysts for Boosting Carbon Dioxide Reduction, *ACS Appl. Energy Mater.* 4 (2021) 2891–2898.
<https://doi.org/10.1021/acsaem.1c00269>.

[42] Y.N. Gong, W. Zhong, Y. Li, Y. Qiu, L. Zheng, J. Jiang, H.L. Jiang, Regulating photocatalysis by spin-state manipulation of cobalt in covalent organic frameworks, *J. Am. Chem. Soc.* 142 (2020) 16723–16731. <https://doi.org/10.1021/jacs.0c07206>.

[43] W. Wan, Y. Zhao, S. Wei, C.A. Triana, J. Li, A. Arcifa, C.S. Allen, R. Cao, G.R. Patzke, Mechanistic insight into the active centers of single/dual-atom Ni/Fe-based oxygen electrocatalysts, *Nat. Commun.* 12 (2021) 1–13. <https://doi.org/10.1038/s41467-021-25811-0>.

[44] B. Wang, J. Tang, X. Zhang, M. Hong, H. Yang, X. Guo, S. Xue, C. Du, Z. Liu, J. Chen, Nitrogen doped porous carbon polyhedral supported Fe and Ni dual-metal single-atomic catalysts: template-free and metal ligand-free synthesis with microwave-assistance and d-band center modulating for boosted ORR catalysis in zinc-air batteries, *Chem. Eng. J.* 437 (2022) 135295. <https://doi.org/10.1016/j.cej.2022.135295>.

[45] L. Jiao, J. Zhu, Y. Zhang, W. Yang, S. Zhou, A. Li, C. Xie, X. Zheng, W. Zhou, S. Yu, H. Jiang, Non-Bonding Interaction of Neighboring Fe and Ni Single-Atom Pairs on MOF-Derived N - Doped Carbon for Enhanced CO₂ Electroreduction, (2021).
<https://doi.org/10.1021/jacs.1c08050>.

[46] O. Bunău, Y. Joly, Self-consistent aspects of x-ray absorption calculations, *J. Phys. Condens. Matter.* 21 (2009). <https://doi.org/10.1088/0953-8984/21/34/345501>.

[47] M.D. Hossain, Z. Liu, M. Zhuang, X. Yan, G.L. Xu, C.A. Gadre, A. Tyagi, I.H. Abidi, C.J. Sun, H. Wong, A. Guda, Y. Hao, X. Pan, K. Amine, Z. Luo, Rational Design of Graphene-Supported Single Atom Catalysts for Hydrogen Evolution Reaction, *Adv. Energy Mater.* 9 (2019) 1–10. <https://doi.org/10.1002/aenm.201803689>.

[48] A. Eckmann, A. Felten, I. Verzhbitskiy, R. Davey, C. Casiraghi, Raman study on defective graphene: Effect of the excitation energy, type, and amount of defects, *Phys. Rev. B - Condens. Matter Mater. Phys.* 88 (2013) 1–11.

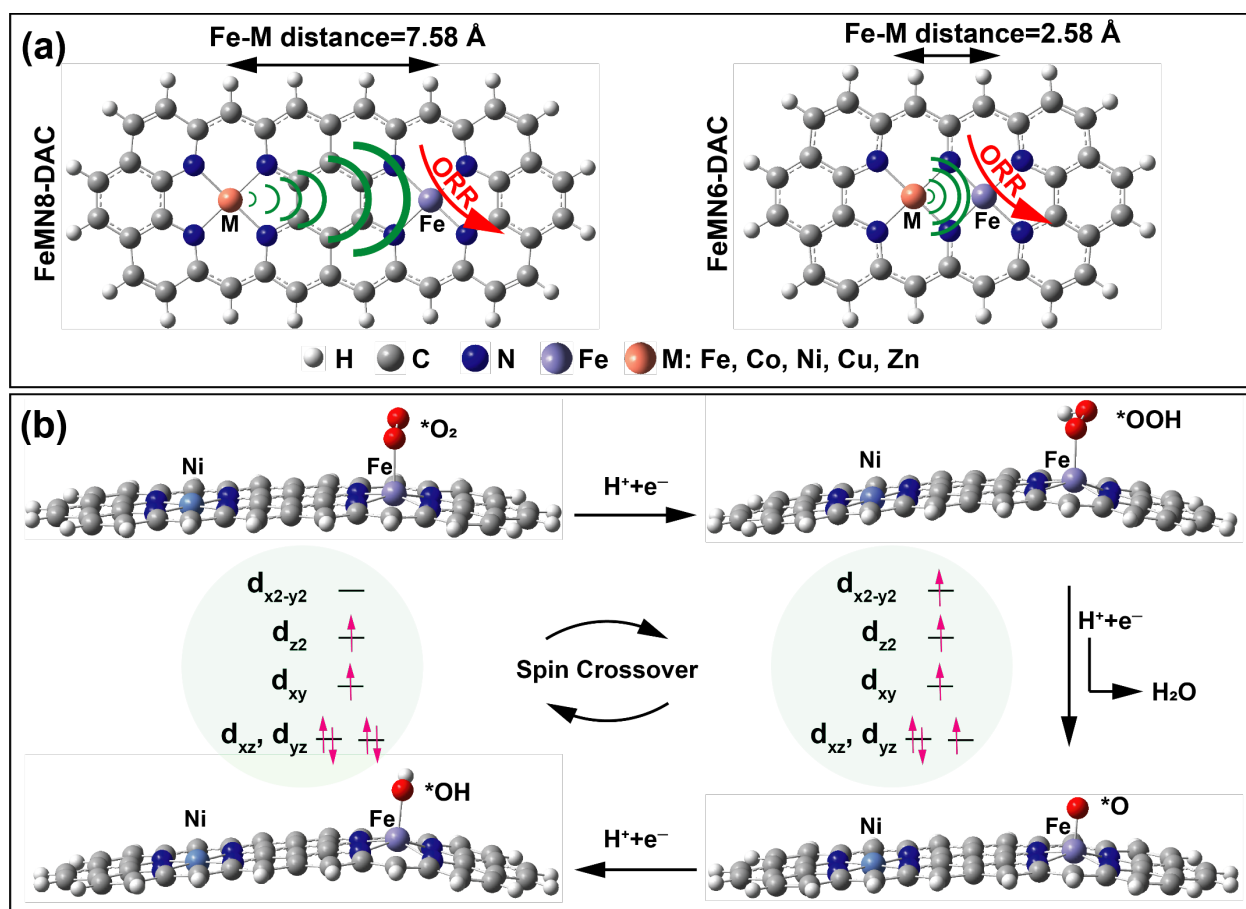
1 <https://doi.org/10.1103/PhysRevB.88.035426>.

- 2 [49] Z. Zhu, H. Yin, Y. Wang, C.H. Chuang, L. Xing, M. Dong, Y.R. Lu, G. Casillas-Garcia,
3 Y. Zheng, S. Chen, Y. Dou, P. Liu, Q. Cheng, H. Zhao, Coexisting Single-Atomic Fe and
4 Ni Sites on Hierarchically Ordered Porous Carbon as a Highly Efficient ORR
5 Electrocatalyst, *Adv. Mater.* 32 (2020) 1–8. <https://doi.org/10.1002/adma.202004670>.

6

7

1



2

3 **Scheme1. Schematic for the application of DACs to ORR.** (a) The structure of FeMN6-DAC
 4 and FeMN8-DAC (Gray colors balls: carbon, dark blue: nitrogen, red: oxygen, cream: hydrogen,
 5 blue: iron, and salmon: counterpart M metal (Fe, Co, Ni, Cu, and Zn)). (b) Lateral view of reaction
 6 intermediates along the ORR pathway for FeNiN8-DAC, indicating the spin crossover during the
 7 reaction. This further indicates the effect of non-bonding effect of counterpart metals on the
 8 catalytic activity of Fe active site.

9

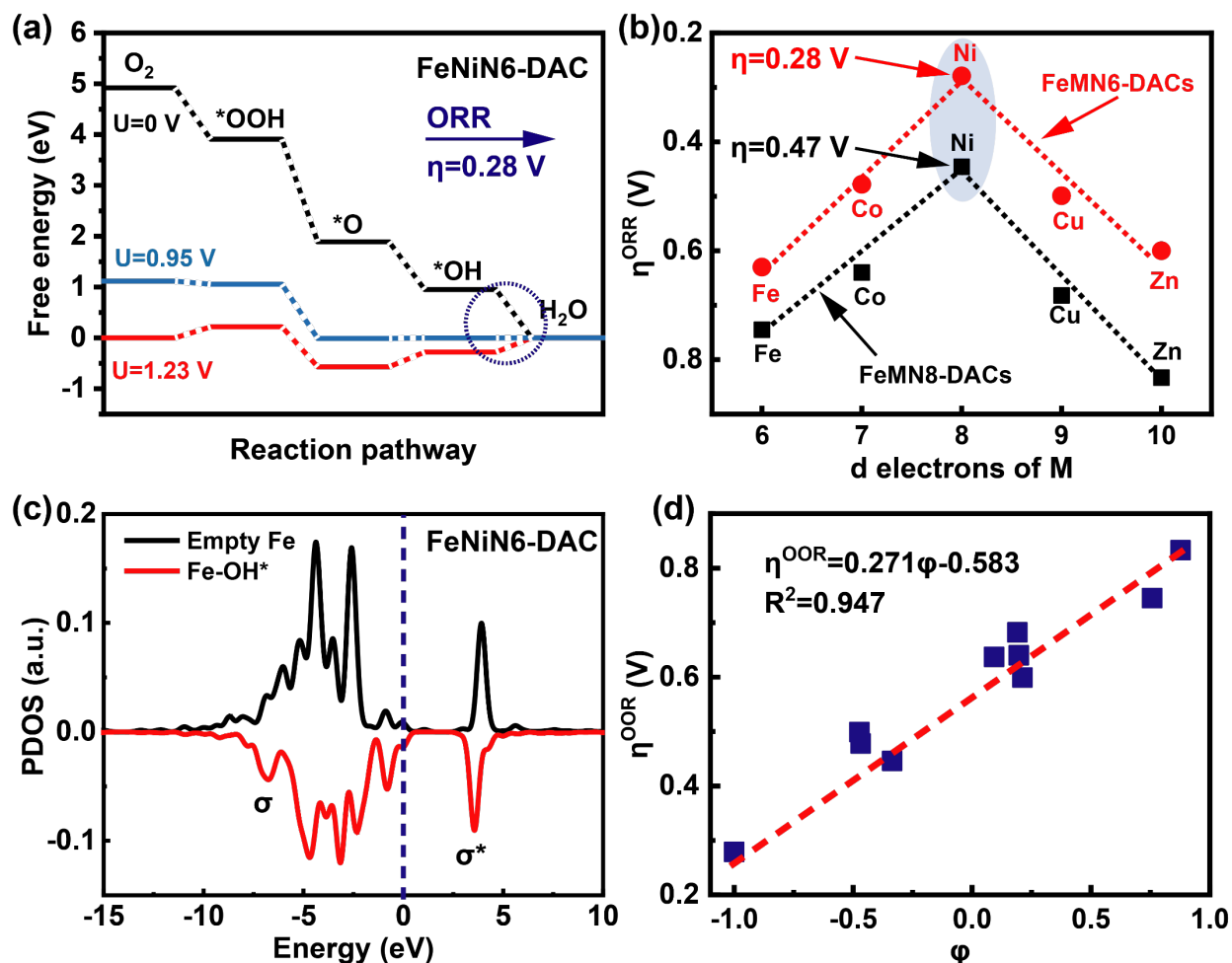


Figure 1. DFT calculations results. (a) The Gibbs free energy diagram for oxygen reduction reaction (ORR) corresponding to FeNiN6-DAC with the ORR overpotentials (η^{ORR}) of 0.28 V, shown in blue circle. (b) Volcano plot of theoretical ORR overpotential (η^{ORR}) versus the d electrons of counterpart metal for FeMN6-DAC and FeMN8-DAC structures, indicating FeNiN6-DAC and FeNiN8-DAC at the summits. (c) PDOS of 3d hybrid orbital of Fe atom in FeNiN6-DAC before and after interaction with OH^* , indicating the bonding (σ) and antibonding (σ^*) orbitals after interaction with OH^* . (d) Overpotential (η^{ORR}) of FeMN6-DAC and FeMN8-DAC versus the new descriptor (ϕ), suggesting the new descriptor satisfactory defines the linear relationship with the η^{ORR} for DACs.

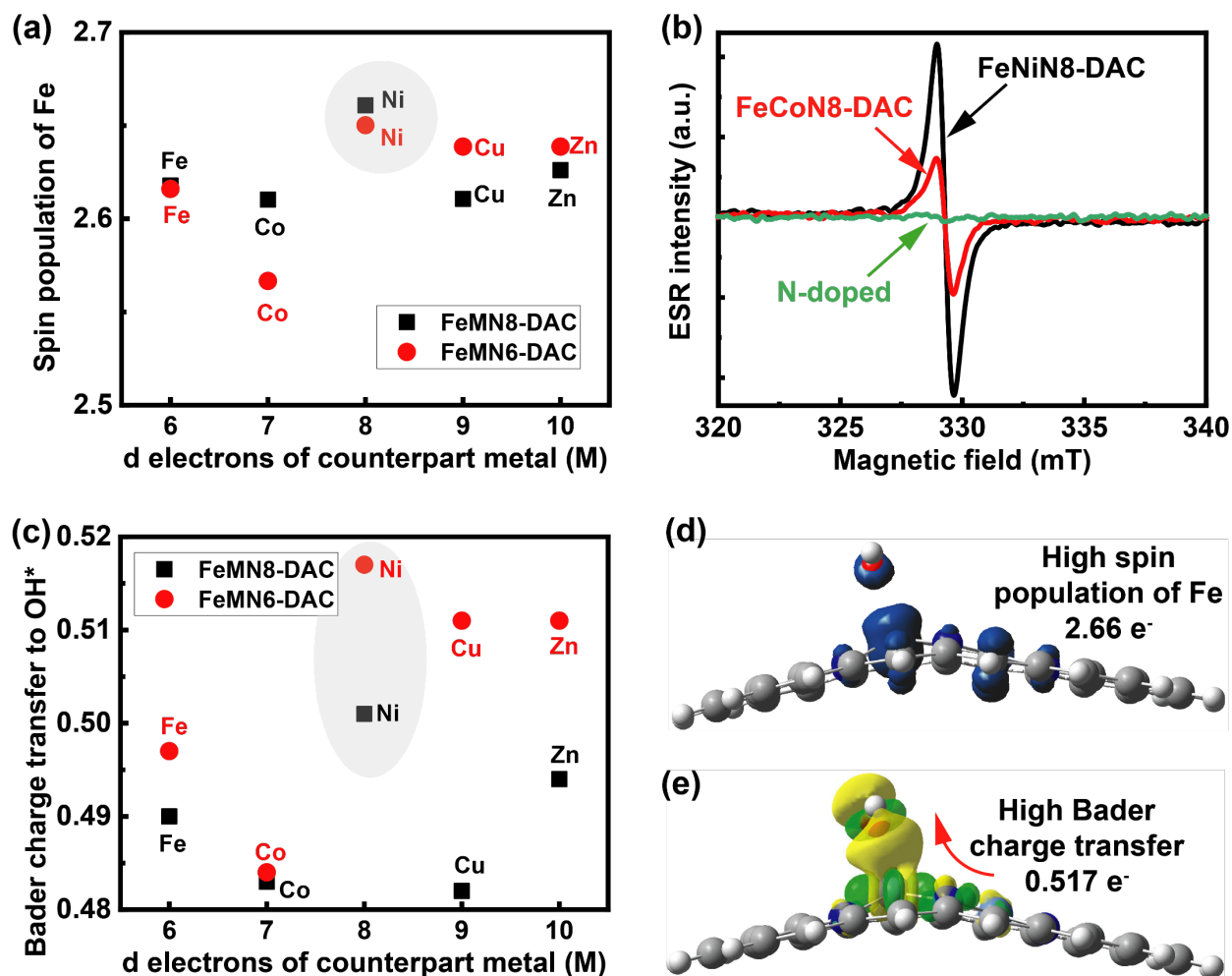


Figure 2. Spin population and Bader charge transfer analysis. (a) The spin population of Fe atom (Fe-OH*) versus d electrons of counterpart metals (M), indicating FeNiN6-DAC and FeNiN8-DAC at the top with higher spin density. (b) Electron spin resonance (ESR) spectra of samples measured at 77 K, indicating higher spin population for FeNiN8-DAC compared to FeCoN8-DAC and no peak for N-doped sample. (c) Bader charge transfer from Fe site to OH* intermediate versus the d electrons of counterpart metal (M). (d) The spatial spin density of FeNiN6-DAC (Isosurface value = 0.015 e/Å³). Blue and green colors represent the alpha and beta spin density, respectively. (e) Side view of charge transfer within the system of FeNiN6-DAC (Isosurface value = 0.004 e/Å³). Yellow and green colors represent the charge availability and deficiency, respectively. This indicates the high spin population and high charge transfer ability of FeNiN6-DAC system.

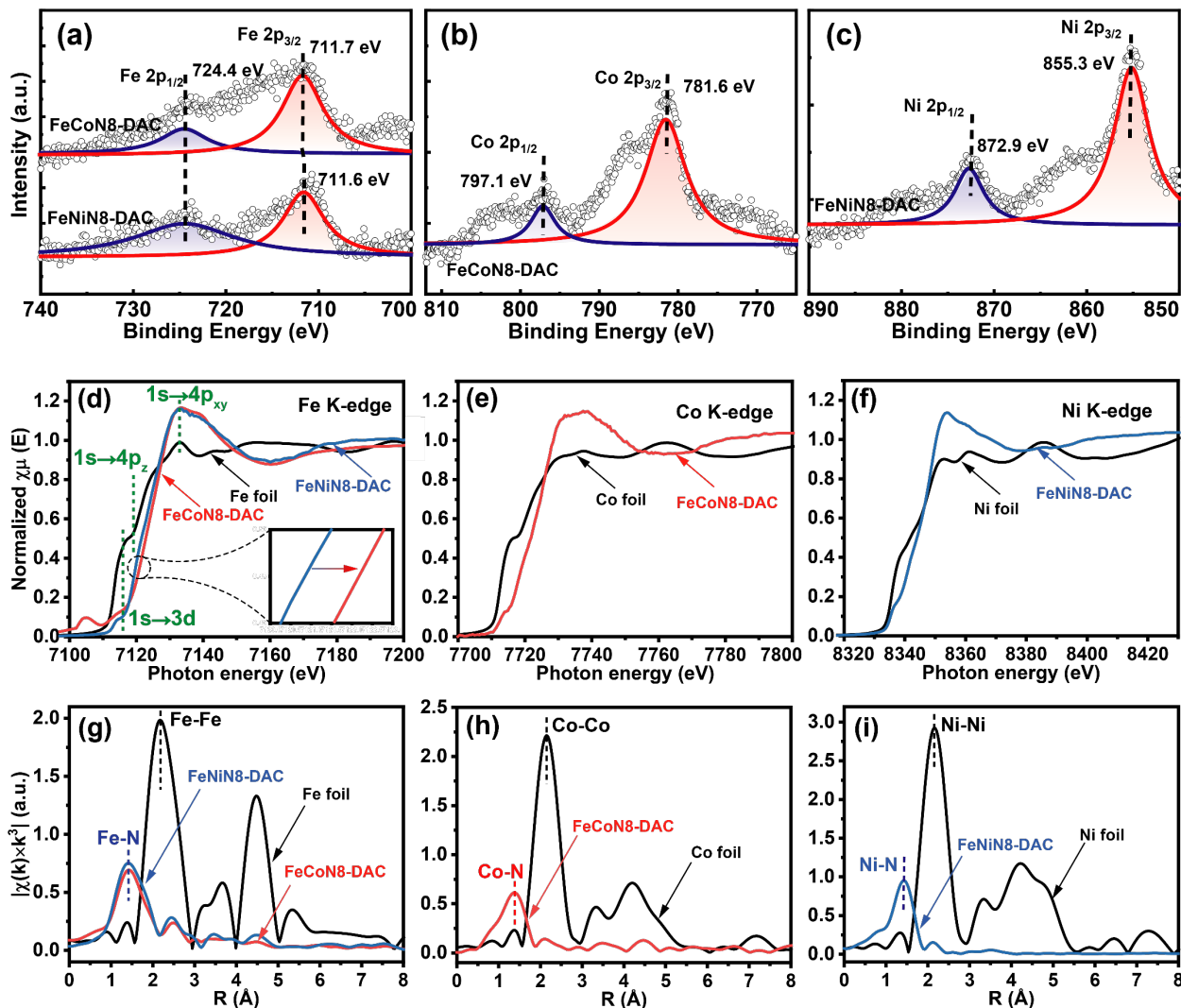


Figure 3. XPS, XANES, and EXAFS characterizations. (a) The Fe 2p, (b) Co 2p, and (c) Ni 2p XPS spectra of synthesized samples, showing two peaks belonging to $2p_{3/2}$ and $2p_{1/2}$. The binding energy of Fe, Co, and Ni indicates their oxidation state of higher than 0. (d) Fe K-edge, (e) Co K-edge, and (f) Ni K-edge XANES spectra of our synthesized samples and their reference bulk samples. Three peaks are corresponded to $1s \rightarrow 3d$, $1s \rightarrow 4p_z$, and $1s \rightarrow 4p_{xy}$ transitions.[40] Fourier transformations (FT) EXAFS spectra in R space of (g) of Fe, (h) Co, and (i) Ni with their reference bulk samples. The primary peaks attributed to Fe-, Co-, and Ni-N are different from Fe-Fe, Co-Co, and Ni-Ni peaks, respectively.

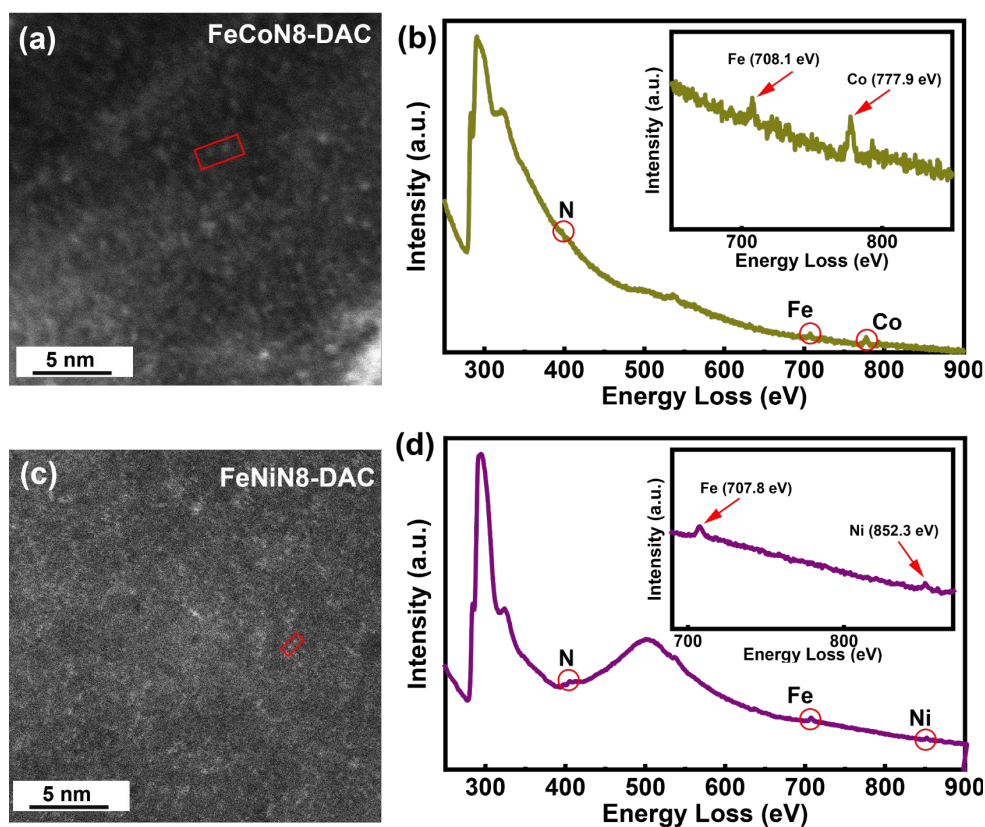


Figure 4. STEM images and EELS characterization. (a) STEM image of the FeCoN8-DAC sample showing that the metal atoms are atomically dispersed on the graphene support. (b) EELS analysis from the dual atoms marked by the red rectangle in (a). (c) STEM image of the FeNiN8-DAC sample showing that the metal atoms are atomically dispersed on the graphene support. (d) EELS analysis from the dual atoms marked by the red rectangle in (c).

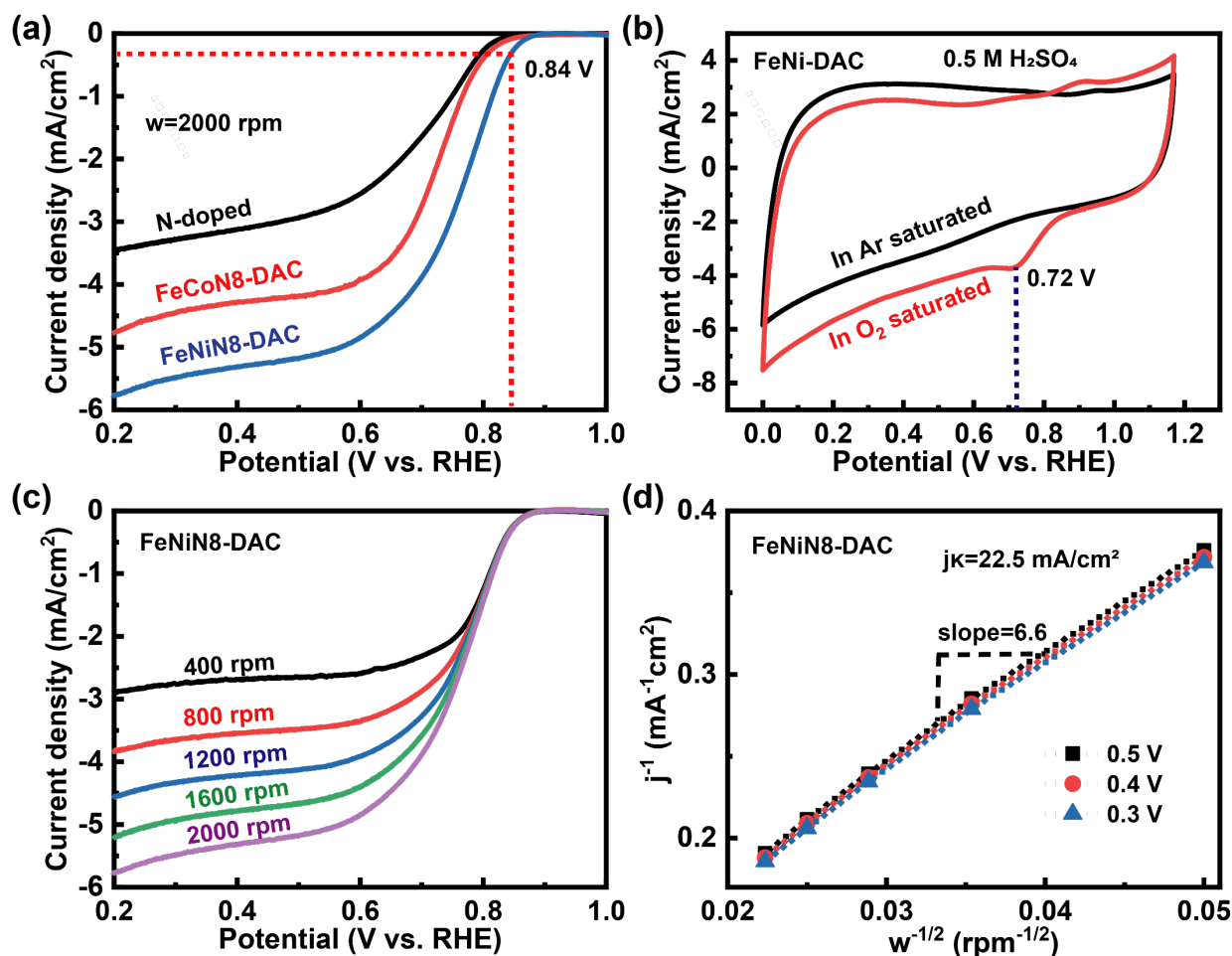


Figure 5. ORR catalytic performance. (a) ORR polarization curves. (b) CV curves for FeNiN8-DAC sample in O₂- and Ar-saturated environment, revealed a prominent ORR peak (red line) at 0.72 V versus RHE. This indicates that O₂ is reduced with the FeNiN8-DAC catalyst. (c) The rotation disk data of the FeNiN8-DAC sample for various rotation speeds. (d) K-L plot for different applied potentials, indicating good linearity with the kinetic current density (j_k) of 22.5 mAcm⁻². All catalytic performance is measured in an O₂-saturated environment using 0.5 M H₂SO₄.

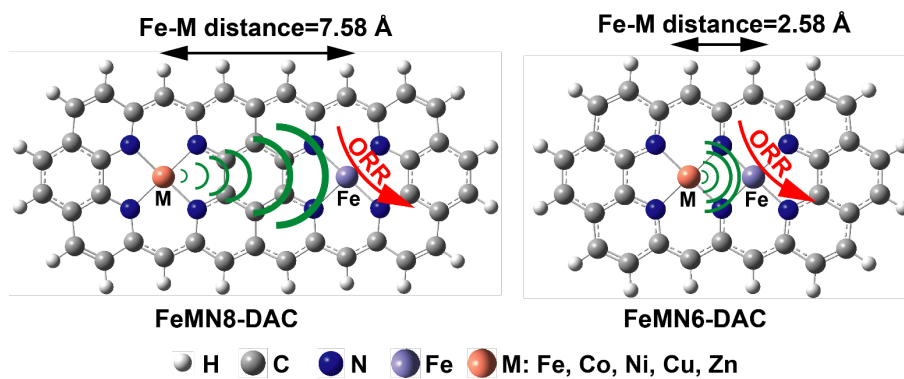


Table of Contents (TOC)